www.MaterialsViews.com

**ADVANCED
ENERGY
MATERIALS**

www.advenergymat.de

COMMUNICATION

# SnSe₂ 2D Anodes for Advanced Sodium Ion Batteries

*Fan Zhang, Chuan Xia, Jiajie Zhu, Bilal Ahmed, Hanfeng Liang, Dhinesh Babu Velusamy, Udo Schwingenschlögl, and Husam N. Alshareef\**

Rechargeable sodium ion batteries (SIBs) have recently attracted a great deal of attention as a promising alternative to lithium ion batteries (LIBs) for large-scale application due to the abundant natural sodium sources and low cost.[1,2] However, despite the fact that sodium displays similar electrochemical properties to lithium, the larger ionic radius of Na$^+$ than Li$^+$ is a crucial factor to the performance of SIB electrodes.[3] To date, different LIBs anode materials have been investigated as anode materials for SIBs, but most efforts have been ineffective due to the low specific capacities and poor cycling performances of these electrodes.[4,5] Take graphite for example, which is a state-of-the-art anode material for commercial LIBs. It can exhibit the lithiation and delithiation process with high reversibility, but has very low electrochemical activity for sodium storage.[6] Hence, appropriate anode materials with high sodium storage ability with excellent cyclic stability and superior rate performance should be studied and developed.

Tin and tin-based compounds, with a high theoretical capacity, have been investigated as the most promising SIBs anode materials.[7,8] The theoretical sodium storage capacity of tin is 847 mA h g$^{-1}$, by alloying reaction, which forms Na$_{15}$Sn$_4$ (Na$_{3.75}$Sn).[9,10] However, tin-based compounds, such as tin oxide (SnO$_2$),[11,12] tin sulfide (SnS$_2$ and SnS),[13,14] and tin selenide (SnSe$_2$ and SnSe),[15] possess higher theoretical capacities than metallic tin, with the additional capacity contribution from conversion reactions. For instance, SnS$_2$ and SnS can deliver a theoretical capacity of 1136 and 1022 mA h g$^{-1}$,[13] respectively, with the mechanism of combination of conversion and alloying reactions. SnSe$_2$ can also deliver a high theoretical capacity of 756 mA h g$^{-1}$ (considering that 1 molar SnSe$_2$ can store 7.75 molar sodium). In spite of high sodium storage ability, the deleterious volume expansion of tin (≈420%) during alloying process seriously damages the cycle stability of tin-based electrodes. In order to solve this problem, preparing composites containing carbon material such as carbon spheres, carbon nanotube, and graphene was carried out by many researches.[16,17] Reduced graphene oxide (RGO), with special 2D structure, large specific surface area, and excellent electronic conductivity, can buffer the large volume changes during alloying reaction.[18,19] Recently, Qu et al. prepared a SnS$_2$/RGO composite as the anode material for SIBs

with a high reversible capacity of 500 mA h g$^{-1}$ at 1 A g$^{-1}$ for 400 cycles and excellent rate performance, which can be attributed to the good conductivity and mechanical resilience of RGO nanocomposites.[14]

SnSe$_2$ is a 2D transition metal chalcogenide material, which has the CdI$_2$-type hexagonal layered structure (a = b = 3.81 Å and c = 6.14 Å, space group P3m1). Within each SnSe$_2$ monolayer, hexagonal closely packed sandwich layers are stacked with a periodicity of one layer tin atom and two layers selenium atoms, and the interlayer spaces are loosely bound by van der Waals bonds. The large interlayer spacing will result in more sodium ion intercalations and buffer the large volume change during sodiation and desodiation processes.[20] Recently, various synthesis methods have been reported to prepare pure SnSe$_2$ material used for photodetector, optoelectronic and energy storage application.[21,22] For example, Zhou et al. synthesized ultrathin SnSe$_2$ flakes on mica substrate in a hot furnace at 600 °C under Ar and H$_2$ atmosphere by chemical vapor deposition method.[21] Fernandes et al. prepared SnSe$_2$ thin film on soda lime glass substrates by selenization of direct current (DC) magnetron sputtered tin metallic precursors in the temperature range from 300 to 579 °C.[23] Choi et al. reported a solution approach using the mixed solvent of oleylamine and dichloromethane at 220 °C.[24] However, all these methods involve complex reaction routes, high temperature, and require some toxic and hazardous reagents, which are not practical for green chemistry synthesis.[25] Beyond that, for the chemical synthesis of selenides, the selenium source mostly used is the hydrazine hydrate solution that has dissolved selenium powder, while hydrazine hydrate is a highly toxic and dangerously unstable reagent.[26,27] Therefore, it is a challenging work to seek a suitable and safe selenium source and a simpler way to prepare pure SnSe$_2$ material.
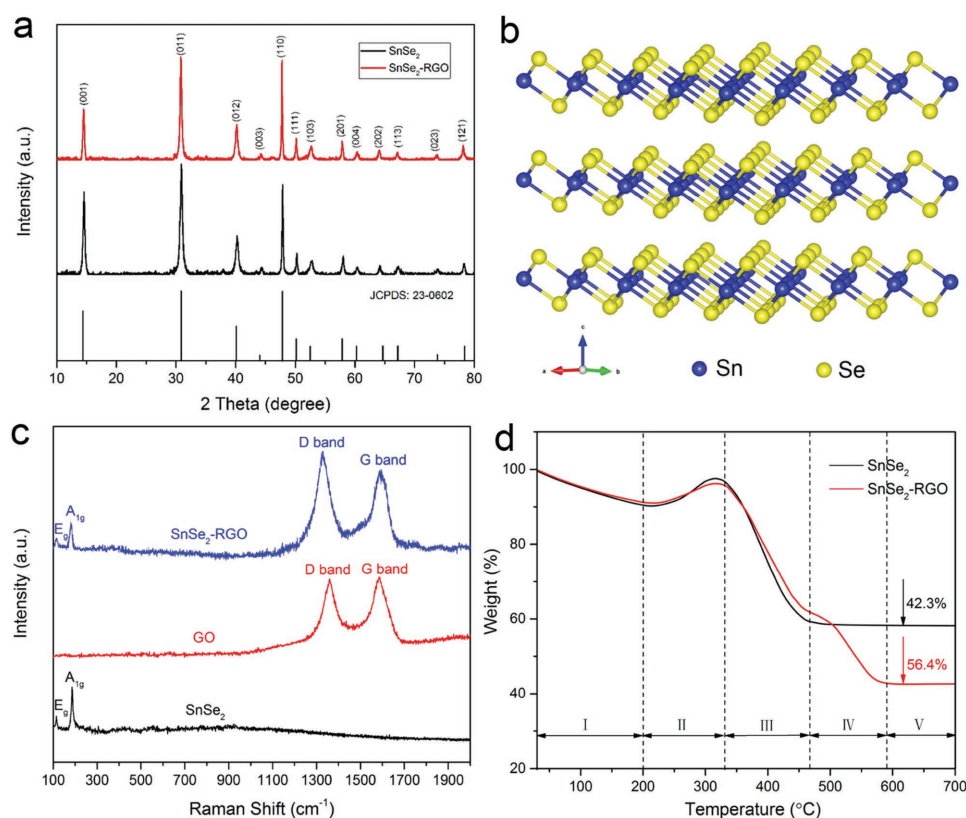
Herein, we report a facile hydrothermal method to prepare pure SnSe$_2$ nanosheets and SnSe$_2$/RGO nanocomposites for the first time, using a safe and stable selenium source, namely, N$_2$ saturated NaHSe solution, with high reaction activity which we exploited. The as-prepared SnSe$_2$ has a layered structure, while the interlayer spacing can accommodate more sodium ions, and the insertion of RGO can improve the electrical conductivity and structure stability of the electrodes. When tested as anode materials for SIBs, the SnSe$_2$/RGO composites exhibit a large reversible capacity of 515 mA h g$^{-1}$ after 100 cycles and excellent rate performances, which are all better than the pure SnSe$_2$ electrode. In addition, the electrochemical mechanism during the cycling process was investigated by ex situ X-ray diffraction (XRD) and high-resolution transmission electron microscopy (HRTEM) analyses, and the role of RGO in buffering the big volume change that takes place during sodium ion intercalations was simulated using density functional theory.

F. Zhang, C. Xia, Dr. J. J. Zhu, B. Ahmed,
Dr. H. F. Liang, Dr. D. B. Velusamy,
Prof. U. Schwingenschlögl, Prof. H. N. Alshareef
Material Science and Engineering
King Abdullah University of Science
and Technology (KAUST)
Thuwal 23955-6900, Saudi Arabia
E-mail: husam.alshareef@kaust.edu.sa

**ADVANCED
ENERGY
MATERIALS**

www.advenergymat.de

Materials
Views

www.MaterialsViews.com

COMMUNICATION

**Figure 1.** a) XRD patterns of pure $SnSe_2$ and $SnSe_2$/RGO nanocomposites. b) Raman spectra of as-prepared pure $SnSe_2$, GO, and $SnSe_2$/RGO nanocomposites. c) Schematic illustration of crystal structure of 2D $SnSe_2$. d) Thermo gravimetric (TG) curves of $SnSe_2$ and $SnSe_2$/RGO.

The crystal structures of the as-synthesized $SnSe_2$ nanosheets and $SnSe_2$/RGO nanocomposites were characterized by the XRD test. As shown in **Figure 1**a, all the diffraction peaks can be assigned to the hexagonal $SnSe_2$ (JCPDS Card no. 23-0602), and the lattice constants of $SnSe_2$ are a = b = 3.81 Å and c = 6.14 Å. The hexagonal layered crystal structure of $SnSe_2$ is shown in Figure 1b. $SnSe_2$/RGO nanocomposites show almost the same diffraction as $SnSe_2$. No peak (001) of graphite oxide (GO) can be observed, suggesting the reduction of GO,[28] and the absence of broad (200) peak of RGO may be due to the $SnSe_2$ nanosheets inhibiting the agglomeration of graphene sheets.[29,30] It is worth mentioning that the selenium source we used is the $N_2$ saturated NaHSe solution was synthesized according to the following equation $4NaBH_4 + 2Se + 7H_2O = 2NaHSe + Na_2B_4O_7 + 14H_2$, and the reason for $N_2$ saturation is that NaHSe can be easily oxidized in the air atmosphere.[25] Raman spectroscopy (Figure 1c) was used to characterize the GO, $SnSe_2$, and $SnSe_2$/RGO samples. The peaks located at 116 and 185 $cm^{-1}$ can be assigned to the $E_g$ and $A_{1g}$ mode of $SnSe_2$,[31] which were present in the spectra of $SnSe_2$ and $SnSe_2$/RGO. The intensity ratio of D-mode and G-mode ($I_D/I_G$) of RGO in $SnSe_2$/RGO sample is 1.22, higher than intensity ratio of GO, which is calculated to be 0.98, indicating that the majority of oxygen-containing groups have been removed and the reduction of the average size of the $sp_2$ domain after GO reduction.[32] In addition, it can be seen that for the $SnSe_2$/RGO composites, the D-band shifts from 1366 to 1343 $cm^{-1}$, while G-band shifts from 1608 to 1602 $cm^{-1}$; the lower frequencies indicate the successful reduction from GO to RGO.[33]

To determine the content of RGO in the nanocomposites, thermogravimetric analysis (TGA) was carried out from 30 to 700 °C at a heating rate of 10 °C $min^{-1}$ in the air. Figure 1d shows the TGA results, in which five steps of weight change can be observed and explained as follows. The first step of weight loss, from room temperature to 200 °C, can be attributed to the evaporation of surface water and the removal of oxygen-containing functional groups from RGO.[34] Then $SnSe_2$ starts to pyrolyze at around 200 °C as $SnSe_2 + 3O_2 = SnO_2 + 2SeO_2$, resulting in nearly 10% weight increment between 200 and 330 °C.[35] After that, $SeO_2$ reaches its sublimation temperature and starts to volatilize, and the weight decreases rapidly until 430 °C, where all the solid $SeO_2$ has volatilized. Then, the step between 430 and 580 °C can be ascribed to the combustion of RGO. For the last step beyond 580 °C, all the final residue is $SnO_2$. The total weight loss of $SnSe_2$/RGO composites is 56.4%, which is equal to the sum of weight loss of $SnSe_2$ and RGO, the weight percentage of RGO in the composites can be calculated from the following formula

$$M \times 56.4\% = M \times X + M \times (1 - X) \times 42.3\%$$

M: the mass of $SnSe_2$/RGO composites; X: the weight percentage of RGO in the composites. Therefore, the accurate weight percentage of RGO in the composites is calculated to be 24.4%, so the mass loading of active materials ($SnSe_2$) is as high as 75.6%, which is significant to the practical application.

www.MaterialsViews.com

ADVANCED
ENERGY
MATERIALS
www.advenergymat.de

COMMUNICATION
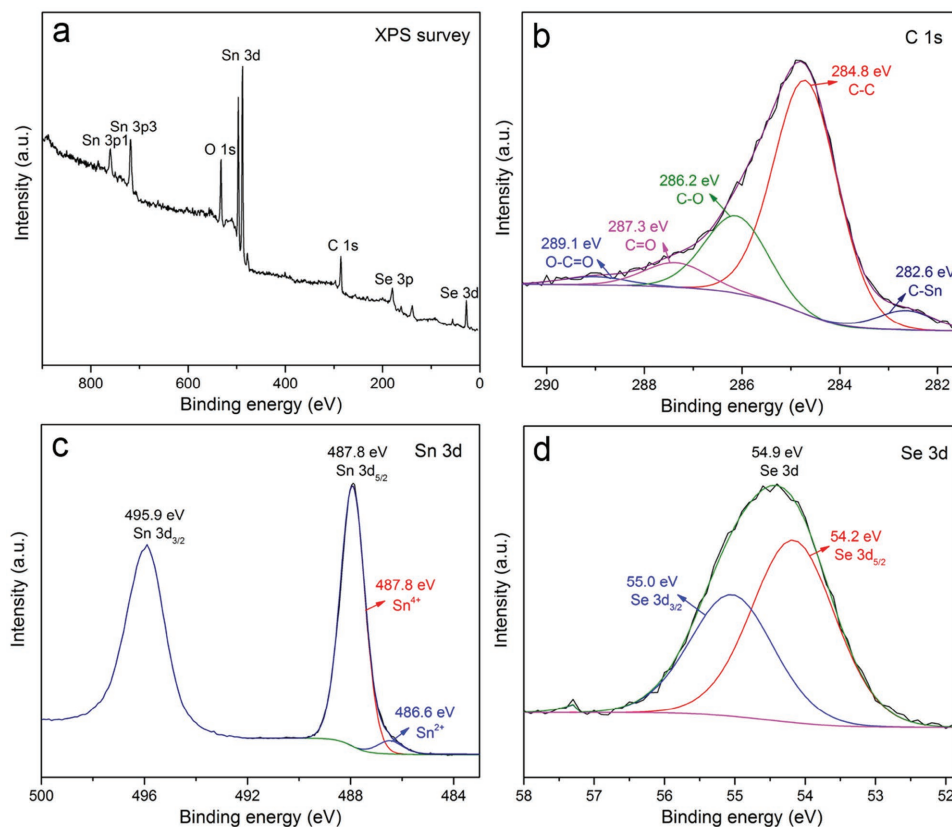
**Figure 2.** XPS spectra of the SnSe$_2$/RGO nanocomposites: a) survey, b) C 1s, c) Sn 3d, and d) Se 3d.
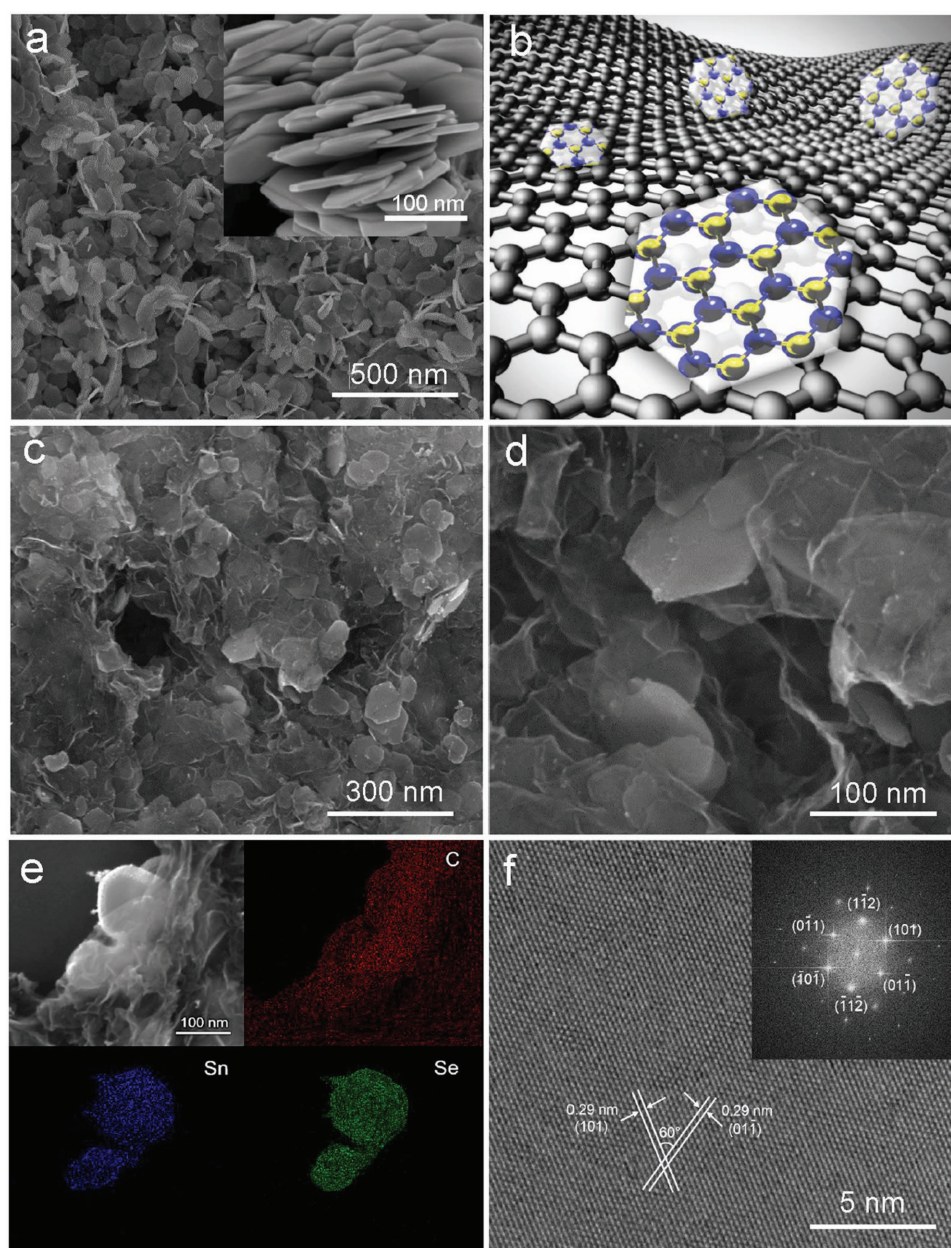
The surface composition of SnSe$_2$/RGO nanocomposites and chemical states of C, Sn, and Se elements was further characterized using X-ray photoelectron spectroscopy (XPS), as shown in **Figure 2**. The survey scan spectrum (Figure 2a) shows that the main elements in SnSe$_2$/RGO nanocomposites are C, Sn, Se, and O. In the high-resolution C 1s spectrum (Figure 2b), the detected peaks can be deconvoluted into five peaks, the carbon in C−C, C−O, C=O, and O−C=O appears at 284.8, 286.2, 287.3, and 289.1 eV, respectively. The strong intensity of C−C peak and low intensities of functional group peaks indicate the extraction of oxygen-involved groups and high reduction of GO.[36] And the peak at 282.6 eV is assigned to carbon in C−Sn bonding. Figure 2c shows the high-resolution spectrum of Sn 3d. Two peaks at 487.8 and 495.9 eV can be ascribed to the Sn 3d$_{5/2}$ and Sn 3d$_{3/2}$ photoelectron emissions respectively. According to the fitting results, Sn$^{2+}$ valence state (486.6 eV) only accounts for a very small section, Sn$^{4+}$ valence state at 487.8 eV is the main part, which means Sn exists principally as the oxidation state of Sn$^{4+}$ and the SnSe$_2$/RGO nanocomposites are well crystallized.[37] Further, in Figure 2d, the binding energies of Se 3d$_{5/2}$ and Se 3d$_{3/2}$ located at 54.2 and 55.0 eV suggest an oxidation state of Se$^{2−}$.[38] Beyond that, the elemental ratio of Sn:Se in SnSe$_2$/RGO is 1:2.05, as demonstrated by the compositional analysis, which is consistent with the stoichiometry of SnSe$_2$.

The morphology and crystal structure of the as-prepared SnSe$_2$ nanosheets and SnSe$_2$/RGO nanocomposites were investigated via scanning electron microscopy (SEM) and

HRTEM. **Figure 3**a shows the SEM images of SnSe$_2$ synthesized by hydrothermal method. As can be seen, SnSe$_2$ forms uniform hexagonal SnSe$_2$ nanosheets, with lateral size in the range of 80–120 nm, and thickness in the range of 10–20 nm. Using our process, we found that SnSe$_2$ nucleates heterogeneously on RGO, which is introduced into the reaction vessel. This process results in uniform SnSe$_2$ growth on the RGO sheets without any aggregation, and SnSe$_2$ maintains its hexagonal morphology (Figure 3c,d). The morphology of SnSe$_2$ nanosheets on 2D reduced graphene oxide was fabricated as schematic illustration described in Figure 3b. Energy-dispersive X-ray spectroscopy (EDX) mapping demonstrates the existence of the elements C, Sn, and Se and the dispersion homogeneities with obvious boundary between hexagonal structure SnSe$_2$ nanosheets and RGO sheets (Figure 3e). The crystal planes of the hexagonal nanosheets were investigated by HRTEM, as shown in Figure 3f. The (101) and (01$\bar{1}$) crystal plan with lattice spacing of 0.29 nm can be observed from the top view of the nanosheets.

In order to confirm the large specific surface area and excellent electronic conductivity of SnSe$_2$/RGO nanocomposite compared with pure SnSe$_2$, N$_2$ adsorption/desorption isotherms were used to obtain the surface area, (as shown in Figure S1, Supporting Information) and four-point probe measurements were performed to obtain the electronic conductivity. Based on the multipoint Brunauer–Emmett–Teller (BET) curves shown in Figure S1 (Supporting Information), we calculated that the specific surface areas of the pure SnSe$_2$ and SnSe$_2$/RGO are

**Figure 3.** a) SEM image of pure SnSe$_2$ at different magnifications. b) Schematic illustration of SnSe$_2$/RGO structure. c,d) Typical SEM image of SnSe$_2$/RGO nanocomposites at different magnifications. e) EDX mapping images of C, Sn, and Se elements with corresponding SEM image. f) HRTEM image of the as-obtained SnSe$_2$ and the corresponding fast Fourier transform (FFT) image.

28.7 and 87.0 m$^2$ g$^{-1}$, respectively, which explains the substantial improvement in SnSe$_2$ performance after the addition of RGO. At room temperature, the electronic conductivity of pure SnSe$_2$ was 3.24 × 10$^{-7}$ S cm$^{-1}$, whereas the conductivity of the SnSe$_2$/RGO nanocomposites was 2.12 × 10$^{-1}$ S cm$^{-1}$, which explains the improved performance of SnSe$_2$ when combined with RGO.

The electrochemical sodium insertion and extraction behaviors of pristine SnSe$_2$ nanosheets and SnSe$_2$/RGO nanocomposites were evaluated using a two-electrode coin cell with sodium metal as the counter electrode. Cycle voltammetry (CV) curves were investigated in the voltage range of 0.005–2.50 V

at the scan rate of 0.2 mV s$^{-1}$ and first, second, third, fifth, and tenth cycles of CV scans are presented in **Figure 4**a,b. For the SnSe$_2$/RGO nanocomposites, as shown in Figure 4b, during the first cathodic scan, the peak at 1.68 and 1.30 V, which disappeared in the subsequent cycles, can be attributed to the sodium intercalation of SnSe$_2$ interlayers without phase decomposition (Equation (1), similar to the lithium and sodium intercalation of SnS$_2$ layers).[14,39] The sharp peak at 0.78 V can be assigned to the conversion and alloying reactions, corresponding to the decomposition of the SnSe$_2$ into metallic Sn and the formation of Na$_2$Se and the alloying reaction between Sn and Na.[40] And the large intensity decrease of peak at 0.78 V in the second
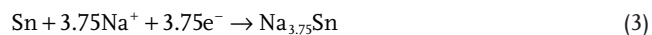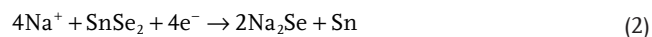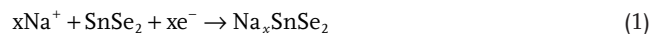
www.MaterialsViews.com

ADVANCED
ENERGY
MATERIALS
www.advenergymat.de

COMMUNICATION
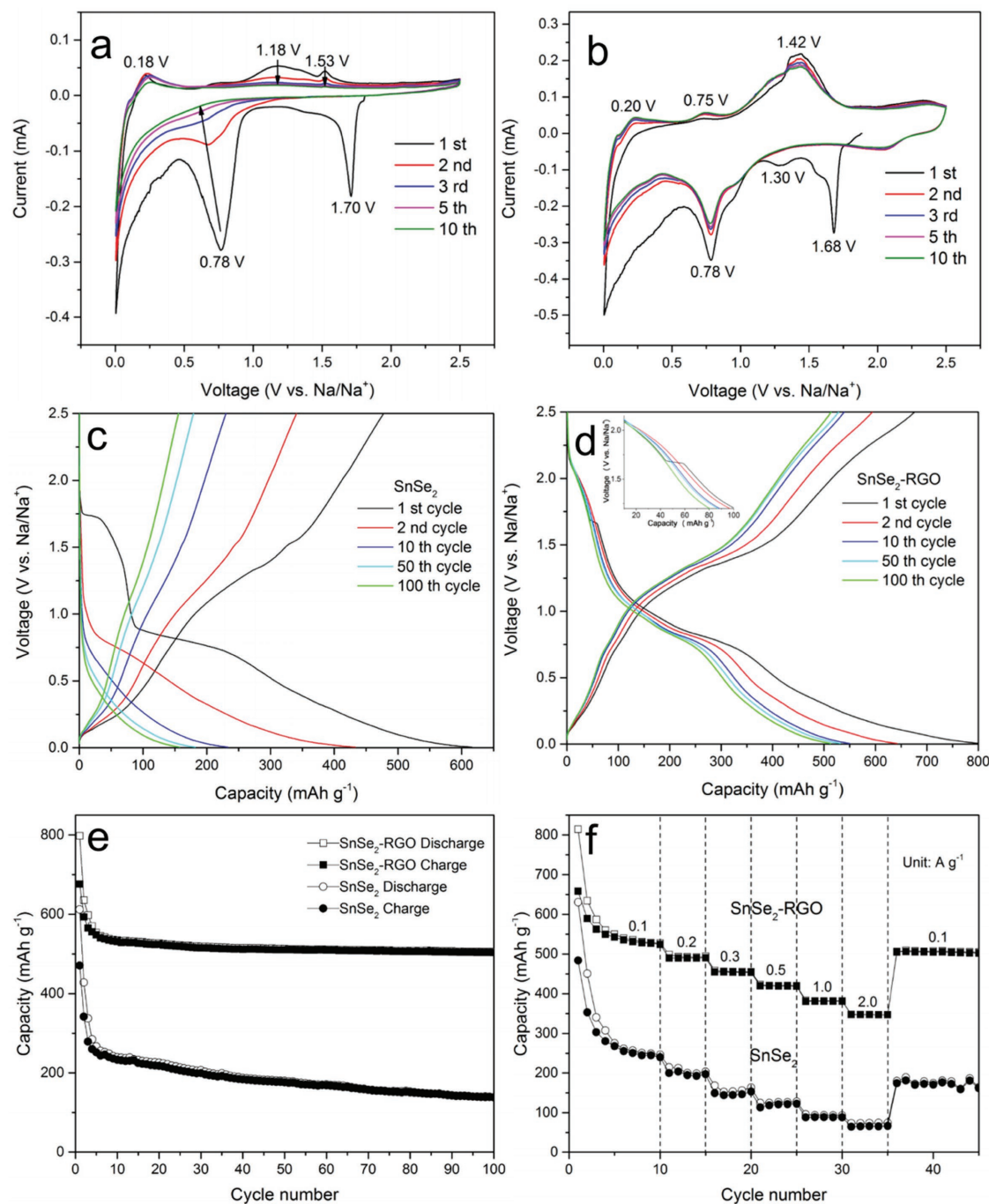
**Figure 4.** a) Cyclic voltammograms of SnSe$_2$ electrode and b) SnSe$_2$/RGO electrode between 0.005 and 2.5 V with a can rate of 0.2 mV s$^{-1}$. c) Galvanostatic charge/discharge profiles of SnSe$_2$ electrode, and d) SnSe$_2$/RGO electrode in the 1$^{st}$, 2$^{nd}$, 10$^{th}$, 50$^{th}$, 100$^{th}$ cycles. e) Cycling performances of SnSe$_2$ and SnSe$_2$/RGO electrodes at 0.1 A g$^{-1}$ for 100 cycles. f) Rate performance of SnSe$_2$ and SnSe$_2$/RGO electrodes.

cycle demonstrates the decomposition of the electrolyte on the surface of nanosized SnSe$_2$ particles and RGO sheets at this voltage, which leads to the formation of irreversible solid electrolyte interface (SEI), related to some irreversible capacity loss and low coulombic efficiency in the first cycle.[41] During first anodic scan, the oxidation peaks at 0.2 and 0.75 V in all cycles can be assigned to the desodiation reaction of Na$_{3.75}$Sn alloy (Equations (2) and (3)).[42] The oxidation peak at 1.42 V can be

ascribed as the restitution of the original SnSe$_2$/RGO nanocomposites. These distinct oxidation peaks correspond to the reversible dealloying reaction and the reformation of SnSe$_2$/RGO. The CV curves for the following ten cycles are superimposed very well with each other, indicating the excellent reversibility of SnSe$_2$/RGO for sodiation and desodiation processes. The CV scan of pristine SnSe$_2$ (Figure 4a) shows similar peaks with SnSe$_2$/RGO composites, indicating the similar electrochemical

reaction. However, it can be readily observed in the tenth cycle of the CV scan that the intensities of pristine $SnSe_2$ decrease rapidly, which corresponds to its poor cyclic performance as compared to $SnSe_2$/RGO composite. The detailed electrochemical reactions are given in Equations (1)–(3)

$$xNa^+ + SnSe_2 + xe^- \rightarrow Na_xSnSe_2 \tag{1}$$

$$4Na^+ + SnSe_2 + 4e^- \rightarrow 2Na_2Se + Sn \tag{2}$$

$$Sn + 3.75Na^+ + 3.75e^- \rightarrow Na_{3.75}Sn \tag{3}$$

To further evaluate the $Na^+$ diffusion performances in the $SnSe_2$/RGO electrode, CV at various scan rates from 0.1 to 2.0 mV s$^{-1}$ was performed in the voltage range of 0.005–2.50 V. As shown in Figure S2 (Supporting Information), the cathodic peaks moved to lower voltages, while the anodic peaks shifted to higher ones when the scan rate was increased. This result can be explained as follows: the redox reactions can happen over the entire active surface area while the scan rate is low; however, at high scan rates, due to the time constraint, the diffusion of $Na^+$ ions will be limited and the electrode will be polarized. Hence, only the outer active surface is effective for redox reactions, which results in the position shift of both reduction and oxidation peaks. The redox peaks were still clearly present in the CV curves of the $SnSe_2$/RGO electrode with increasing scan rate up to 2.0 mV s$^{-1}$, indicating excellent reversibility of the $Na^+$ extraction-insertion reaction and good electronic conductivity of the $SnSe_2$/RGO electrode.[43]

Figure 4c,d shows the galvanostatic charge/discharge profiles of pristine $SnSe_2$ nanosheets and $SnSe_2$/RGO nanocomposite electrodes in the 1st, 2nd, 10th, 50th, and 100th cycles at a current density of 0.1 A g$^{-1}$ in the potential range of 0.005–2.50 V. The charge/discharge voltage plateaus are consistent with observations made in CV scans. For the $SnSe_2$/RGO electrode (Figure 4d), the initial discharge plateau located at 1.70 V corresponds to the intercalation of sodium ions into $SnSe_2$ interlayers, but it disappears after the first cycle, which confirms this $Na^+$ intercalation process is irreversible. The second discharge plateau located at 0.78 V is ascribed to the conversion and alloying reactions. During the first desodiation process, the small voltage plateau and broad voltage plateau located at 0.75 and 1.40 V are consistent with the dealloying of $Na_{3.75}Sn$ and restitution of the original $SnSe_2$/RGO structure, respectively, revealing the highly reversibility of the electrode. The $SnSe_2$/RGO nanocomposites exhibit a high first discharge capacity of 798 mA h g$^{-1}$ (a little higher than the theoretical capacity 756 mA h g$^{-1}$) and charge capacity of 660 mA h g$^{-1}$. The electrode materials may not be fully involved in the sodiation process if the irreversible capacity generated from the electrolyte decomposition and SEI formation were taken into consideration.[44] From second cycle, the shape of charge/discharge profiles is similar, indicating the sodium storage is highly reversible, and after 100 cycles, the $SnSe_2$/RGO nanocomposites exhibit a high reversible capacity of 515 mA h g$^{-1}$, indicating a high stability of the electrode. The $SnSe_2$ electrode can deliver an initial discharge and charge capacity of 621 and 465 mA h g$^{-1}$ (Figure 4c), which are lower than the $SnSe_2$/RGO

electrode, and the shape of profiles changes distinctly during the following cycling, suggesting a lower reversibility and structural stability during the sodiation and desodiation processes.

Figure 4e depicts the cycling performances of as-synthesized pristine $SnSe_2$ and $SnSe_2$/RGO composites electrodes at a current density of 0.1 A g$^{-1}$ between 0.005 and 2.50 V. The initial discharge and charge capacities of $SnSe_2$/RGO composites are 798 and 660 mA h g$^{-1}$, respectively, corresponding to a coulombic efficiency (CE) of 83%, the first cycle capacity loss pertains to the formation of SEI film formation.[45] After first cycle, CE increases quickly to over 99% and remains at nearly 100% thereafter, revealing a high stability of SEI formed on anode/electrolyte interface during the first cycle.[46] The $SnSe_2$/RGO electrode demonstrates excellent cycling stability and reversibility in the following cycles. After 100 cycles, a reversible capacity as high as 515 mA h g$^{-1}$ was maintained. The galvanostatic charge/discharge profile and cycle performance of pure RGO are shown in the Figure S3 (Supporting Information), where it is clear that they exhibit low capacity (53 mA h g$^{-1}$ after 100 cycles at the current density of 0.1 A g$^{-1}$). This result means that pure RGO makes negligible contribution to the overall capacity of the $SnSe_2$/RGO electrode. By contrast, cells made of pristine $SnSe_2$ electrode show a lower initial capacity of 621 mA h g$^{-1}$ for discharging and 465 mA h g$^{-1}$ for charging and a reversible capacity of 152 mA h g$^{-1}$ after 100 cycles. The poor cycle performance and reversible capacity are mainly due to the low conductivity and huge volume change of unsupported $SnSe_2$ and the aggregation of Sn or $Na_{3.75}Sn$ nanoparticles during the cycling process.[24] The obvious difference between pristine $SnSe_2$ and $SnSe_2$/RGO electrodes suggests that after the insertion of conductive RGO into $SnSe_2$ nanosheets, the formation of 3D network architecture with nanosized $SnSe_2$ sheets will improve the conductivity of the composites. RGO can be considered as an ideal supporting matrix for the transportation and storage of sodium ions due to its high intrinsic surface and flexibility, and it will buffer the big volume change and prevent nanosized particles aggregation during the sodiation and desodiation processes.[16] Thereby, compared with the pristine $SnSe_2$ electrode, the $SnSe_2$/RGO composite electrodes exhibited a higher capacity and an excellent cyclic performance.

Moreover, the $SnSe_2$/RGO electrode also exhibited excellent rate capability when tested at high current densities. Figure 4f shows the rate performances of the pristine $SnSe_2$ and $SnSe_2$/RGO electrodes at different current densities between 0.1 and 2 A g$^{-1}$. With the current densities increasing from 0.1 to 0.2, 0.3, 0.5, 1.0, 2.0 A g$^{-1}$, the $SnSe_2$/RGO electrodes exhibit good capacity retention, varying from 528 to 504, 485, 440, 398, 365 mA h g$^{-1}$, respectively. And a reversible capacity of 520 mA h g$^{-1}$, almost without capacity loss, can be achieved after the rate returns to 0.1 A g$^{-1}$, which is much larger than the pristine $SnSe_2$ electrode. The pristine $SnSe_2$ electrode only maintains a specific capacity of 82 mA h g$^{-1}$ at the 2.0 A g$^{-1}$, and when current density is reduced to 0.1 A g$^{-1}$, only a reversible capacity of 172 mA h g$^{-1}$ is maintained. These results demonstrate that the $SnSe_2$/RGO nanocomposites with high electrical conductivity and large specific surface area can allow the transformation of sodium ions at high current density without irreversible change of 3D hybrid structure.[47]

www.MaterialsViews.com

**ADVANCED
ENERGY
MATERIALS**
www.advenergymat.de

COMMUNICATION

The electrochemical impedance spectroscopy (EIS) was carried out to better understand the reaction kinetics and electrical conductivities of $SnSe_2$ electrode with and without RGO. Figure S4 (Supporting Information) shows the Nyquist plots of pure $SnSe_2$ nanosheets and $SnSe_2$/RGO nanocomposites; the inset shows the equivalent circuit model fitting with the experimental results. The semicircle in the high frequency region is associated with the charge-transfer resistance $R_{ct}$ and the double-layer capacitance of electrode–electrolyte interface $C_{d1}$. The straight sloping line in the low frequency region corresponds to the sodium ion diffusion process. It can be readily observed that $SnSe_2$/RGO electrode has a smaller semicircle diameter ($R_{ct}$ = 45 Ω) as compared with $SnSe_2$ electrode ($R_{ct}$ = 120 Ω), indicating that $SnSe_2$/RGO has higher electrical conductivity and faster reaction kinetics. This result can be attributed to the large contact area between electrode and electrolyte in the presence of RGO.

The mechanism of stability of $SnSe_2$/RGO electrode was further studied by ex situ SEM imaging. The SEM images of pristine $SnSe_2$ and $SnSe_2$/RGO electrodes and the same electrodes after 100 cycles one are shown in the Figure S5 (Supporting Information). As we can see, after 100 cycles, the structure of $SnSe_2$ electrodes had been totally destroyed; by contrast, the hexagonal nanosheet morphology of $SnSe_2$/RGO was maintained, even though the surfaces and boundaries of $SnSe_2$ crystal in $SnSe_2$/RGO composite became blurred, indicating good structural stability of the $SnSe_2$/RGO composite.

In order to further clarify the electrochemical mechanism and the reversible structure conversions upon the sodiation and desodiation processes, ex situ XRD and HRTEM analyses of the $SnSe_2$/RGO electrode at various discharge and charge states in the first cycle were carried out. As shown in **Figure 5**a, the fresh electrode (state A) shows a clear XRD pattern of the pure $SnSe_2$ lattice with the peak located at 43.5°, which is attributed to the copper current collector. When the cell is discharged to 1.70 V (state B), the XRD pattern shows nothing different except the decrease of peak intensities and broadening of peaks, corresponding to the intercalation process of $Na^+$ into $SnSe_2$ forming $Na_xSnSe_2$. During the insertion of $Na^+$, the interlayer spaces between $SnSe_2$ monolayers can be opened and crystal structure of $SnSe_2$ breaks down gradually. This is because the $SnSe_2$ layers cannot provide enough space for too many $Na^+$ ions. With increasing interlayer spacing,[37] the crystal structure will become amorphous, consistent with broadening of peaks and decreasing of intensities. Upon discharging to 1.2 V (state C), the electrode becomes almost totally amorphous and no distinct peaks can be detected. After further discharging to 0.78 V (state D), the existence of $β$-Sn and $Na_2Se$ can be observed by their characteristic peaks at 30.6° and 37.5° in the XRD pattern, and their crystal structures can be found in the ex situ HRTEM image (Figure S6a, Supporting Information), indicating the conversion reaction from $SnSe_2$ to $β$-Sn and $Na_2Se$ at an initial stage of the $Na^+$ reaction. Following the gradual conversion reaction, alloying reaction will occur simultaneously, forming $Na_xSn$ ($x$ = 3.75).[13] After fully discharging to 0.005 V (state E), the $Na_2Se$ peak intensities become stronger, but beyond that, two broad peaks located at around 18.5° and 32.5° appear, corresponding to the sodiated Sn phase as $Na_xSn$ and the very small crystallite size of the alloy.[48] After reverse charging to

1.05 V (state F), the $Na_xSn$ phase signals disappear and $β$-Sn signal becomes stronger, indicating the dealloying reaction of Na-Sn crystalline particles and the reappearance of metallic Sn. When the electrode is charged to 1.42 V (state G), the peak intensities corresponding to $SnSe_2$ increase, while $β$-Sn and $Na_2Se$ decrease gradually, which can be assigned to the recombination of $β$-Sn and $Na_2Se$, generating $SnSe_2$. Finally, after fully charging to 2.5 V (state H), the peaks of $β$-Sn and $Na_2Se$ almost disappear, where only nanosized $SnSe_2$ exists, which is also demonstrated by the ex situ HRTEM results (Figure S6b, Supporting Information). The lattice fringes of $SnSe_2$, Sn, and $Na_2Se$ can be found and the nanosized $SnSe_2$ is the main component, indicating a high electrochemical reaction reversibility; it is worth mentioning that the selected area electron diffraction (SAED) pattern indicates a polycrystalline nature of $SnSe_2$ due to its nanoscale size. The result indicates that during sodiation and desodiation processes, the $SnSe_2$/RGO electrode can retain its crystal and chemical structure, and the existence of RGO can relieve the aggregation and restacking of nanosized $SnSe_2$, which will be contributing to the high reversible capacity and remarkable cycling performances.

Based on all the experimental evidences, the oxidation and reduction mechanism along the discharge and charge processes can be ascribed in the schematic illustration of Figure 5b. During discharging, the $Na^+$ will intercalate into $SnSe_2$ interlayers first at around 1.70 V, leading to the expansion of crystal structure. After that, the conversion reaction will happen, the hexagonal $SnSe_2$ will transfer into a face-centered tetragonal $β$-Sn and a cubic $Na_2Se$, and alloying reaction occurs subsequently between $β$-Sn and Na, forming orthorhombic $Na_{3.75}Sn$ nanocrystal, resulting in a broad peak at 0.78 V. During charging, the electrode will undergo the inverse reaction of alloying and conversion, and $SnSe_2$ will be reformed, suggesting a high reversibility of the electrochemical reaction. Literature data on the performances of transition metal selenide as anode materials for SIBs are presented in Table S1 (Supporting Information)[49–53] and promising performances of them have been demonstrated by Zhang et al.[54] and Cho et al.[55] Among all of these transition metal selenides, $SnSe_2$ has the highest theoretical sodium storage capacity of 756 mA h g$^{-1}$, benefiting from the mechanism of combination of conversion and alloying reactions. And we also demonstrate, for the first time, the performance of $SnSe_2$ and $SnSe_2$/graphene nanocomposites as anodes for sodium ion batteries. A high initial discharge capacity of 798 mA h g$^{-1}$ and reversible specific capacity of 515 mA h g$^{-1}$ at 0.1 A g$^{-1}$ after 100 cycles and an excellent rate performance have been achieved.

As we know, the large volumetric changes that occur during the charge/discharge process of tin-based materials result in electrical disconnection from the conductive medium (e.g., Super P) and current collectors (e.g., Cu foil), which severely affects the stability of the electrode.[56] $SnSe_2$, as a 2D material, may tolerate the volumetric changes caused by sodiation and desodiation processes thanks to its layered crystal structure. **Figure 6**a illustrates the structure change of $SnSe_2$ and $SnSe_2$/RGO after sodium ion intercalation, and Figure 6b shows the simulation results for the lattice expansion of $Na_xSnSe_2$ ($0 \leq x \leq 2$) as the function of the number of Na atoms per unit cell. When $x \leq 1$, the volume increases very slowly for pristine
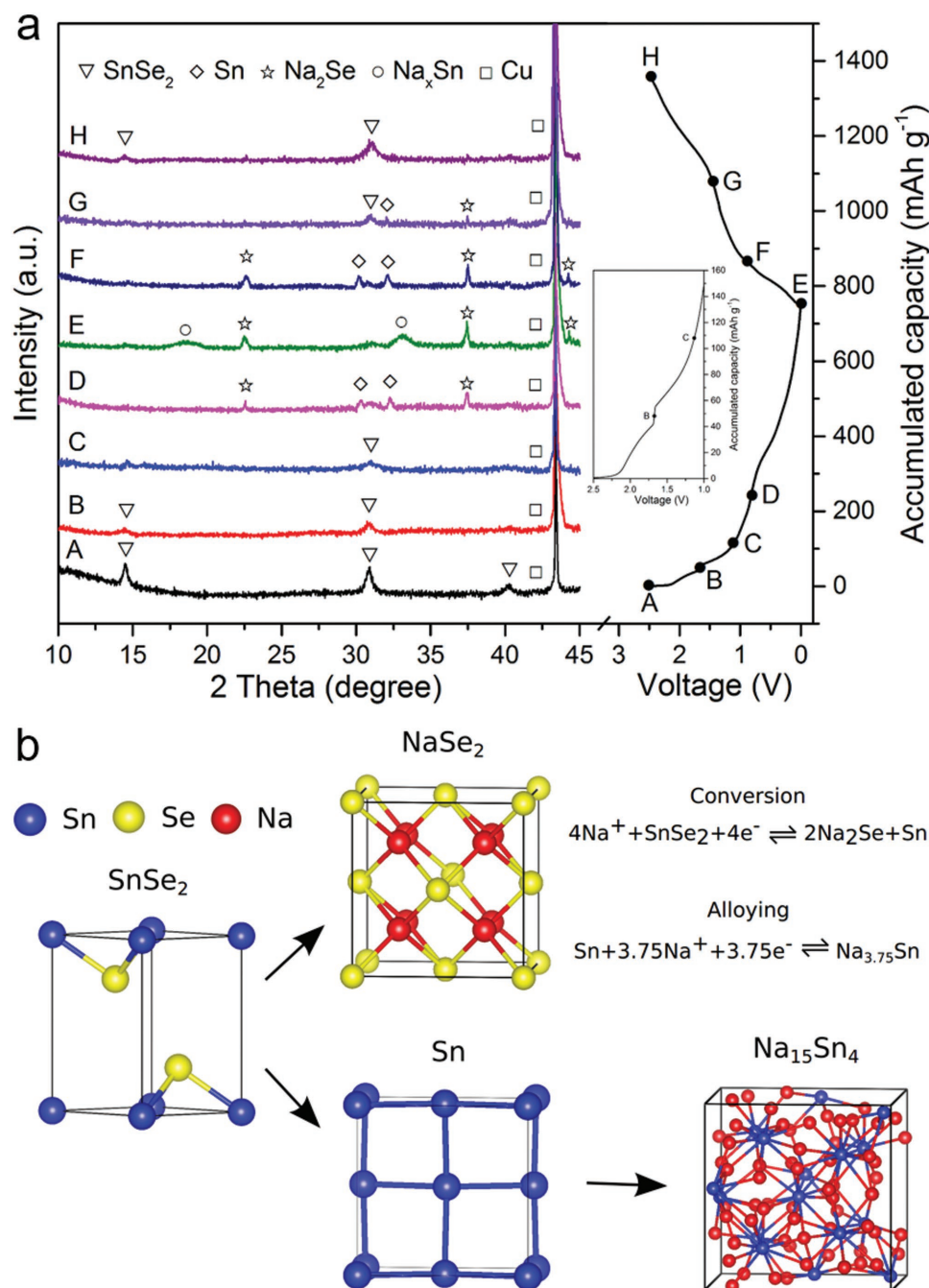
**Figure 5.** a) Ex situ XRD patterns of the SnSe$_2$/RGO electrode collected at different discharge/charge states as indicated in the corresponding voltage profile. (A) fresh electrode, (B) discharge to 1.70 V, (C) discharge to 1.20 V, (D) discharge to 0.78 V, (E) discharge to 0.005 V, (F) charge to 1.05 V, (G) charge to 1.42 V, (H) charge to 2.50 V. b) Schematic illustration of the structure evolution during the sodiation process.

SnSe$_2$ and SnSe$_2$/RGO composites, with lattice expansions 0.5% and 3.5%, respectively. When the Na content is higher than 1 ($x > 1$), the volume of pristine SnSe$_2$ increases swiftly, but the SnSe$_2$/RGO composite still shows very small expansions. Finally, when the electrode is sodiated to Na$_2$SnSe$_2$, the lattice expansions of pristine SnSe$_2$ and SnSe$_2$/RGO composites increase to 17.5% and 1.0%, respectively. This result is consistent with experimental data, and we can therefore conclude that the large intrinsic surface area of RGO is an appropriate supporting matrix for SnSe$_2$ nanosheets. Hence, RGO effectively buffers the volume change of SnSe$_2$ and maintains stability of the electrode structure.

In summary, we have demonstrated a simple way to prepare pure SnSe$_2$ nanosheets and SnSe$_2$/RGO nanocomposites with a new selenium source. The well-developed SnSe$_2$/RGO anodes are believed to function synergistically to stabilize the structure and improve the conductivity of the electrodes. When utilized as anode materials for Na ion batteries, the SnSe$_2$/RGO nanocomposites

www.MaterialsViews.com

ADVANCED
ENERGY
MATERIALS
www.advenergymat.de

COMMUNICATION
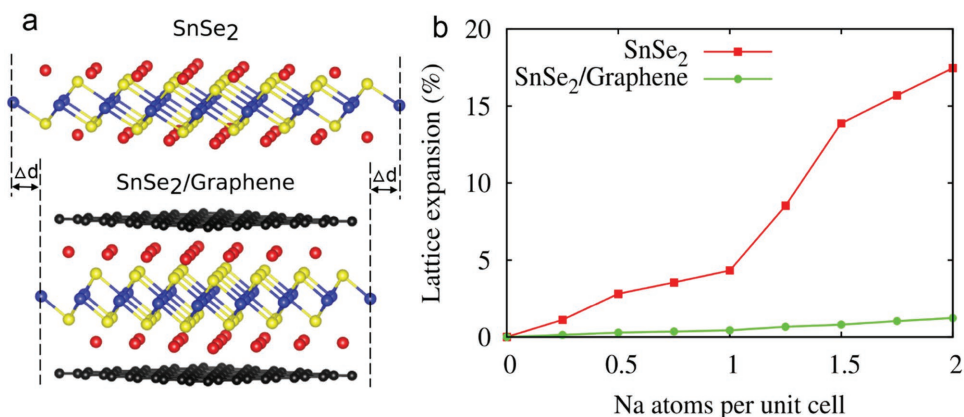
**Figure 6.** a) Schematic illustration of structure change of $SnSe_2$ and $SnSe_2$/RGO after sodium ion intercalation. b) Lattice expansion as a function of Na atoms per unit cell.

deliver a high initial capacity of 798 mA h g$^{-1}$ and still exhibit a reversible capacity of 515 mA h g$^{-1}$ at 0.1 A g$^{-1}$ after 100 cycles. Furthermore, an excellent rate performance has been demonstrated. This study provides experimental and theoretical evidence for the mechanism of electrochemical sodium storage in $SnSe_2$. These results indicate that $SnSe_2$ is a promising candidate for high-performance sodium ion batteries.

## Experimental Section

*Preparation of GO and RGO*: The graphite oxide was prepared by a modified Hummer's method,[57] as-synthesized graphite oxide was dispersed in water by sonication for 3 h to give a brown solution (0.1 mol L$^{-1}$). The reduction of graphene oxide was carried out with the assistance of hydrazine hydrate (35 wt% in water) and ammonia solution (28 wt% in water).[58] In a typical procedure, 150.0 µl of hydrazine solution and 1 mL ammonia solution were added into the 100 mL homogeneous dispersed graphene oxide solution in a 200 mL glass beaker, which was put into a 95 °C water bath and stirred for 1 h. Color of the solution would turn black gradually, which suggested the successful reduction of graphene oxide to reduced graphene oxide.

*Preparation of Pure $SnSe_2$ and $SnSe_2$/RGO Composites*: A typical synthesis procedure of $SnSe_2$/RGO composites is given as follows: 0.176 g $SnCl_4 \times 5H_2O$ (0.5 mmol) was added to 5 mL deionized water (DI water) under stirring as the tin source. Then, 0.08 g $NaBH_4$ (2 mmol) was dissolved in 5 mL $N_2$ statured DI water in a glass bottle, after that, 0.08 g Se powder (1 mmol) was added into the bottle with protective $N_2$ or Argon atmosphere under gentle shaking until the Se powder totally dissolved and a clear transparent solution was obtained, which was used as the selenium source NaHSe solution. Next, 5 mL tin source and 5 mL selenium source were mixed with 30 mL $N_2$ statured RGO solution (≈35 mg RGO) and stirred for 30 min. Finally, the mixture was transferred to a 50 mL Teflon-lined stainless steel autoclave and heated in an electric oven at 180 °C for 24 h. After cooling to room temperature, the obtained product was collected by centrifugation, washed with DI water and ethanol several times and dried at 60 °C for 12 h under vacuum. Pure $SnSe_2$ was prepared with the same route but without the presence of RGO in the precursor.

*Material Characterization*: The phase composition and elemental presence were identified using XRD spectra by a Bruker diffractometer (D8 Advance) with Cu K$\alpha$ radiation at a scanning speed of 5° min$^{-1}$ and X-ray photoelectron spectroscopy (X486.6 eV) X-ray source. Raman spectra were taken on a Hariba LabRAM HR spectrometer with He-Ne laser at 633 nm. The TGAs were carried out on the Netzsch TG 209 F1 instrument from 30 to 700 °C at a heating rate of 10 °C min$^{-1}$ in the air. The morphology of the products was characterized by SEM

on a FEI Nova Nano 630 microscope and HRTEM by the FEI Titan 80–300 KV microscope. The BET surface area and pore size distribution were identified by nitrogen adsorption and desorption using ASAP 2420 (Surface area and pore size analyzer, Micromeritics) at a bath temperature of −195.85 °C. Electronic conductivity was characterized by the MET-007 4 point probe. The electrodes characterized by ex situ XRD were obtained by dissembling the cycled batteries at various voltages in an argon-filled glovebox, any residual salt on the surface of electrodes was moved by washing the cycled electrodes with battery grade dimethyl carbonate (DMC) several times and dried at 80 °C for 2 h under vacuum.

*Electrochemical Measurements*: The homogeneous slurry was prepared by mixing the active materials ($SnSe_2$ or $SnSe_2$/RGO), carbon black (Super P), and polyvinylidene difluoride binder in a 7:1.5:1.5 weight ratio in n-methyl-2-pyrrolidone. Then, the slurry was uniformly pasted on a copper current collector and dried at 80 °C in a vacuum oven over 24 h, the typical active material mass was ≈1.2 mg. For electrochemical measurement, CR2032-type coin half-cells, using sodium foil as the counter electrode, were assembled in an argon-filled glove box, where both $H_2O$ and $O_2$ concentrations were less than 1 ppm. The separator were Celgard 3501 microporous membranes, and the electrolyte was 1 M solution of $NaClO_4$ dissolved in ethylene carbonate/DMC with 1:1 weight ratio. Cyclic voltammetry was measured by a Biologic VMP3 electrochemistry workstation in the voltage range of 0.005–2.5 V (V vs Na/Na$^+$) at a scan rate of 0.2 mV s$^{-1}$ to examine the reduction and oxidation peaks. The galvanostatic discharge and charge at different current density states were performed by an Arbin BT-2043 battery testing system between the voltage range of 0.005–2.5 V. EIS measurements were conducted by applying a sine wave with amplitude of 5.0 mV over the frequency range from 1000 kHz to 0.01 Hz at open-circuit voltage.

*Computational Methods*: Total energy calculations were carried out in the framework of density functional theory using the projector augmented wave method as implemented in the Vienna Ab-initio Simulation Package.[59] The generalized gradient approximation of Perdew, Burke, and Ernzerhof is selected for the exchange-correlation potential,[60] and the long-range interlayer interaction is described by the DFT-D3 method.[61] Moreover, the plane wave was set to 500 eV. The self-consistent calculations were converged to 10$^{-6}$ eV, and the atomic forces to 0.01 eV Å$^{-1}$. A 6 × 6 × 6 k-mesh was employed for the Brillouin zone integrations. 2 × 2 × 1 supercells were built to investigate the sodiation processes, with a vacuum layer of 15 Å thickness added to avoid artificial interaction between periodic images.

## Supporting Information

Supporting Information is available from the Wiley Online Library or from the author.

## Acknowledgements

[1] D. Larcher, J. Tarascon, *Nat. Chem.* **2015**, *7*, 19.

[2] S. W. Kim, D. H. Seo, X. Ma, G. Ceder, K. Kang, *Adv. Energy Mater.* **2012**, *2*, 710.

[3] Y. Zhu, X. Han, Y. Xu, Y. Liu, S. Zheng, K. Xu, L. Hu, C. Wang, *ACS Nano* **2013**, *7*, 6378.

[4] S. P. Ong, V. L. Chevrier, G. Hautier, A. Jain, C. Moore, S. Kim, X. Ma, G. Ceder, *Energy Environ. Sci.* **2011**, *4*, 3680.

[5] M. D. Slater, D. Kim, E. Lee, C. S. Johnson, *Adv. Funct. Mater.* **2013**, *23*, 947.

[6] Y. Wen, K. He, Y. Zhu, F. Han, Y. Xu, I. Matsuda, J. Ishii, J. Cumings, C. Wang, *Nat. Commun.* **2014**, *5*, 4033.

[7] Z. Li, J. Ding, D. Mitlin, *Acc. Chem. Res.* **2015**, *48*, 1657.

[8] H. Zhu, Z. Jia, Y. Chen, N. Weadock, J. Wan, O. Vaaland, X. Han, T. Li, L. Hu, *Nano Lett.* **2013**, *13*, 3093.

[9] J. W. Wang, X. H. Liu, S. X. Mao, J. Y. Huang, *Nano Lett.* **2012**, *12*, 5897.

[10] V. L. Chevrier, G. Ceder, *J. Electrochem. Soc.* **2011**, *158*, A1011.

[11] D. Su, H.-J. Ahn, G. Wang, *Chem. Commun.* **2013**, *49*, 3131.

[12] M. Gu, A. Kushima, Y. Shao, J.-G. Zhang, J. Liu, N. D. Browning, J. Li, C. Wang, *Nano Lett.* **2013**, *13*, 5203.

[13] T. Zhou, W. K. Pang, C. Zhang, J. Yang, Z. Chen, H. K. Liu, Z. Guo, *ACS Nano* **2014**, *8*, 8323.

[14] B. Qu, C. Ma, G. Ji, C. Xu, J. Xu, Y. S. Meng, T. Wang, J. Y. Lee, *Adv. Mater.* **2014**, *26*, 3854.

[15] Y. Kim, Y. Kim, Y. Park, Y. N. Jo, Y.-J. Kim, N.-S. Choi, K. T. Lee, *Chem. Commun.* **2015**, *51*, 50.

[16] Y. Zhao, X. Li, B. Yan, D. Li, S. Lawes, X. Sun, *J. Power Sources* **2015**, *274*, 869.

[17] Y. Denis, P. V. Prikhodchenko, C. W. Mason, S. K. Batabyal, J. Gun, S. Sladkevich, A. G. Medvedev, O. Lev, *Nat. Commun.* **2013**, *4*, 2922.

[18] Y. Lin, X. Han, C. J. Campbell, J. W. Kim, B. Zhao, W. Luo, J. Dai, L. Hu, J. W. Connell, *Adv. Funct. Mater.* **2015**, *25*, 2920.

[19] C. Chen, H. Xu, T. Zhou, Z. Guo, L. Chen, M. Yan, L. Mai, P. Hu, S. Cheng, Y. Huang, *Adv. Energy Mater.* **2016**, *6*, 1600322.

[20] X. Huang, Z. Zeng, H. Zhang, *Chem. Soc. Rev.* **2013**, *42*, 1934.

[21] X. Zhou, L. Gan, W. Tian, Q. Zhang, S. Jin, H. Li, Y. Bando, D. Golberg, T. Zhai, *Adv. Mater.* **2015**, *27*, 8035.

[22] Y. Huang, K. Xu, Z. Wang, T. A. Shifa, Q. Wang, F. Wang, C. Jiang, J. He, *Nanoscale* **2015**, *7*, 17375.

[23] P. Fernandes, M. Sousa, P. M. Salome, J. Leitao, A. da Cunha, *CrystEngComm* **2013**, *15*, 10278.

[24] J. Choi, J. Jin, I. G. Jung, J. M. Kim, H. J. Kim, S. U. Son, *Chem. Commun.* **2011**, *47*, 5241.

[25] C. Xia, Q. Jiang, C. Zhao, M. N. Hedhili, H. N. Alshareef, *Adv. Mater.* **2016**, *28*, 77.

[26] Z. Zhang, X. Yang, Y. Fu, K. Du, *J. Power Sources* **2015**, *296*, 2.

[27] H. Tang, K. Dou, C.-C. Kaun, Q. Kuang, S. Yang, *J. Mater. Chem. A* **2014**, *2*, 360.

[28] L. Tang, Y. Wang, Y. Li, H. Feng, J. Lu, J. Li, *Adv. Funct. Mater.* **2009**, *19*, 2782.

[29] Y. Zhang, P. Zhu, L. Huang, J. Xie, S. Zhang, G. Cao, X. Zhao, *Adv. Funct. Mater.* **2015**, *25*, 481.

[30] G. Williams, B. Seger, P. V. Kamat, *ACS Nano* **2008**, *2*, 1487.

[31] J. Yu, C. Y. Xu, Y. Li, F. Zhou, X. S. Chen, P. A. Hu, L. Zhen, *Sci. Rep.* **2015**, *5*, 17109.

[32] B. Qu, C. Ma, G. Ji, C. Xu, J. Xu, Y. S. Meng, T. Wang, J. Y. Lee, *Adv. Mater.* **2014**, *26*, 3854.

[33] Z.-S. Wu, W. Ren, L. Gao, B. Liu, C. Jiang, H.-M. Cheng, *Carbon* **2009**, *47*, 493.

[34] P. Cui, J. Lee, E. Hwang, H. Lee, *Chem. Commun.* **2011**, *47*, 12370.

[35] Y. Huang, H. Lu, H. Gu, J. Fu, S. Mo, C. Wei, Y.-E. Miao, T. Liu, *Nanoscale* **2015**, *7*, 18595.

[36] Y. Jiang, M. Wei, J. Feng, Y. Ma, S. Xiong, *Energy Environ. Sci.* **2016**, *9*, 1430.

[37] W. Sun, X. Rui, D. Yang, Z. Sun, B. Li, W. Zhang, Y. Zong, S. Madhavi, S. Dou, Q. Yan, *ACS Nano* **2015**, *9*, 11371.

[38] J. Yao, B. Liu, S. Ozden, J. Wu, S. Yang, M.-T. F. Rodrigues, K. Kalaga, P. Dong, P. Xiao, Y. Zhang, *Electrochim. Acta* **2015**, *176*, 103.

[39] X. Jiang, X. Yang, Y. Zhu, J. Shen, K. Fan, C. Li, *J. Power Sources* **2013**, *237*, 178.

[40] Y. N. Ko, S. H. Choi, S. B. Park, Y. C. Kang, *Nanoscale* **2014**, *6*, 10511.

[41] X. Zhou, L. J. Wan, Y. G. Guo, *Adv. Mater.* **2013**, *25*, 2152.

[42] C. Zhai, N. Du, H. Zhang, J. Yu, D. Yang, *ACS Appl. Mater. Interfaces* **2011**, *3*, 4067.

[43] Z. Tong, H. Lv, X. Zhang, H. Yang, Y. Tian, N. Li, J. Zhao, Y. Li, *Sci. Rep.* **2015**, *5*, 16864.

[44] C. K. Chan, X. F. Zhang, Y. Cui, *Nano Lett.* **2008**, *8*, 307.

[45] C. K. Chan, H. Peng, G. Liu, K. McIlwrath, X. F. Zhang, R. A. Huggins, Y. Cui, *Nat. Nanotechnol.* **2008**, *3*, 31.

[46] K. Tang, L. Fu, R. J. White, L. Yu, M. M. Titirici, M. Antonietti, J. Maier, *Adv. Energy Mater.* **2012**, *2*, 873.

[47] Y. Yan, Y. X. Yin, Y. G. Guo, L. J. Wan, *Adv. Energy Mater.* **2014**, *4*, 8.

[48] Y. Kim, Y. Kim, A. Choi, S. Woo, D. Mok, N. S. Choi, Y. S. Jung, J. H. Ryu, S. M. Oh, K. T. Lee, *Adv. Mater.* **2014**, *26*, 4139.

[49] Z. A. Zhan, X. X. Zhao, J. Li, *Mater. Lett.* **2016**, *162*, 169.

[50] S. H. Choi, Y. C. Kang, *Nanoscale* **2016**, *8*, 4209.

[51] H. Wang, X. Z. Lan, D. L. Jiang, Y. Zhang, H. H. Zhon, Z. P. Zhang, Y. Jiang, *J. Power Sources* **2015**, *283*, 187.

[52] D. Xie, W. J. Tang, Y. D. Wang, X. H. Xia, Y. Zhong, D. Zhou, D. H. Wang, X. L. Wang, J. P. Tu, *Nano Res.* **2016**, *9*, 1618.

[53] K. Share, J. Lewis, L. Oakes, R. E. Carter, A. P. Cohn, Cary L. Pint, *RSC Adv.* **2015**, *5*, 101262.

[54] K. Zhang, Z. Hu, X. Liu, Z. L. Tao, J. Chen, *Adv. Mater.* **2015**, *27*, 3305.

[55] J. S. Cho, S. Y. Lee, Y. C. Kang, *Sci. Rep.* **2016**, *6*, 23338.

[56] G. Derrien, J. Hassoun, S. Panero, B. Scrosati, *Adv. Mater.* **2007**, *19*, 2336.

[57] W. S. Hummers Jr., R. E. Offeman, *J. Am. Chem. Soc.* **1958**, *80*, 1339.

[58] D. Li, M. B. Mueller, S. Gilje, R. B. Kaner, G. G. Wallace, *Nat. Nanotechnol.* **2008**, *3*, 101.

[59] G. Kresse, J. Furthmüller, *Phys. Rev. B* **1996**, *54*, 11169.

[60] J. P. Perdew, K. Burke, M. Ernzerhof, *Phys. Rev. Lett.* **1996**, *77*, 3865.

[61] S. Grimme, J. Antony, S. Ehrlich, H. Krieg, *J. Chem. Phys.* **2010**, *132*, 154104.